AISTech 2019 — Proceedings of the Iron & Steel Technology Conference
6–9 May 2019, Pittsburgh, Pa., USA
DOI 10.1000.377.224

3D Thermal-Mechanical Model of Solidifying Steel Strand

M.L.S. Zappulla[1], G. Zhu[2], and B.G. Thomas[1]

[1] Colorado School of Mines
Department of Mechanical Engineering
1500 Illinois St, Golden, Colorado, 80401, USA
Phone: 303-273-3309
Email: bgthomas@mines.edu

[2] University of Science and Technology Beijing
Department of Materials Processing and Control Engineering
No. 30 Xueyuan Road, Beijing 100083, P.R. China
Email: zhuguoming@ustb.edu.cn

Keywords**:** Solidification, Continuous Casting, Secondary Cooling, Thermal-mechanical, Stress, bending, unbending, bulging, roll contact, Finite Element Modeling

INTRODUCTION

In harsh environments such as steel continuous casting, computational modeling is an important tool for process understanding and improvement. Thermal-mechanical models are important to understanding the formation of cracks, depression, and other related casting defects. Large scale and highly refined models are computationally expensive and difficult to validate, however, especially in three dimensions (3D). Lots of information can be obtained from simplified 2D models, as many previous works are, however, 3D models introduce the ability to explore more phenomena such as corner effects, stresses in the casting direction, and the complicated behavior in the bending and unbending regions. Some previous 3D models have focused on solidification in casters but with an emphasis on grain morphology as related to hot tearing [1]. Some models have used a combined 2D and 3D technique in multiphase simulations [2], [3], however these models are mostly relegated to the mold region and neglect the rest of the caster. A small subset of work has explored bulging [4]–[7] or unbending [8] [9] and a few studied both together [10]–[12]. Furthermore in many cases these are simplified or limited in dimension, domain, simulation length, or application. While many of these models have focused on stresses in secondary cooling, some have also explored the heat transfer in smaller scale models and laboratory studies [13]–[15]. The large models sometimes neglect much in the way of heat transfer from spray cooling and roll contacts making it difficult to study the effects of non-uniformities that can drastically affect the cyclic loading that the strand surface experiences [16]. Some recent 3D models have examined heat transfer and stress in a slab caster, but the stress calculation and solidification stress models were uncoupled [17]. Another focused specifically on individual sprays, heat transfer and solidification, but neglected stresses [18].

This work follows a 3D chunk of steel from its molten state, as it moves down through the caster, and experiences primary solidification in the mold, secondary cooling in the spray zones, along with interactions with the support rolls, bending and unbending, and bulging between rolls as a result of ferrostatic pressure. The model includes phase-, temperature-, carbon content-, and strain-rate-dependent, constitutive equations; as well as temperature-dependent thermal properties.

MODEL SETUP

The 3D model of a thick slab caster was developed in LS-DYNA [19] using a combined Lagrangian and Eulerian reference methodology. In this methodology, the Eulerian domain of the caster (mold walls and support-roll surfaces) is fixed in space, which provides the mechanical contact boundary conditions for the Lagrangian domain of the strand chunk, which travels down through the caster at the typical constant casting speed of 1.04 m/min. As shown in Figure 1, the model includes a 2.4 m long chunk of the strand that is 1000 mm wide and 158 mm thick, assuming symmetry about the vertical centerplane

through the strand thickness, so only half (500 mm) of the width is simulated. As the initial condition, the strand chunk is completely liquid, positioned above the meniscus level in the mold, as shown in the second frame of Figure. 1. This chunk travels down through the 0.8 m working mold length and 16 m of the secondary cooling zones.

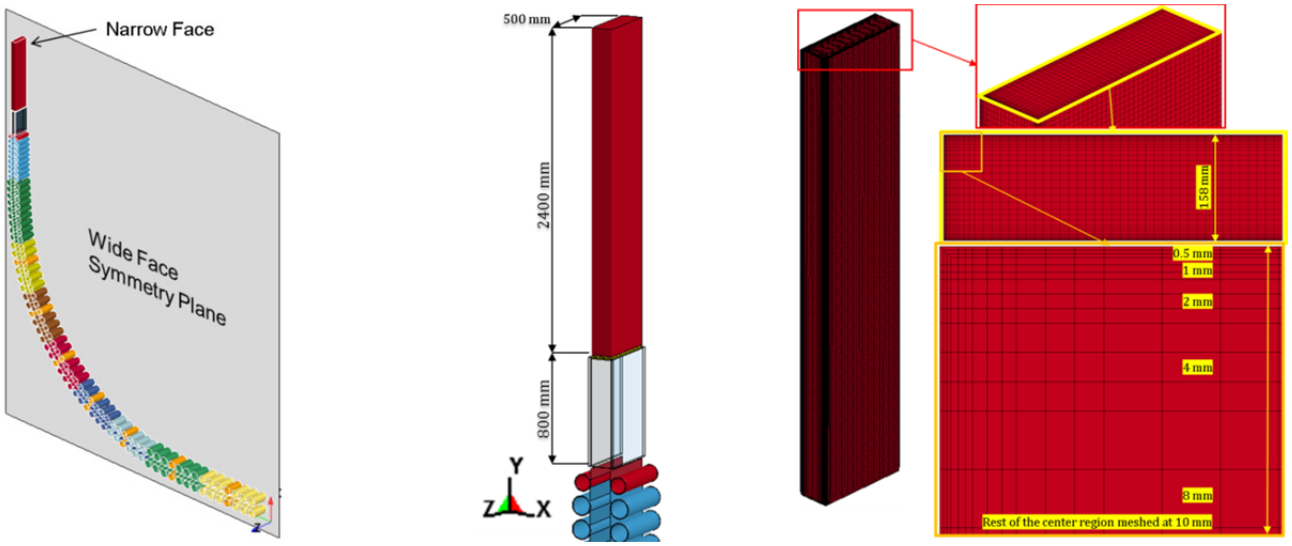

Figure 1: Computational model domain of half-caster showing rolls, chunk domain in initial position, and mesh

Thermal Boundary Conditions

The initial temperature of the entire strand is set to 1550 °C, representing the pour temperature of molten steel entering the mold at the meniscus, as shown in Figure 2. Each node in the domain above the meniscus stays fixed at the pour temperature until the time when it enters the working mold region, at which time its temperature degree-of-freedom is enabled. The initial temperature of the dummy bar is set to 700 °C. Heat transfer within the mold is imposed using thermal contact conductance and a fixed mold temperature of 200 °C.

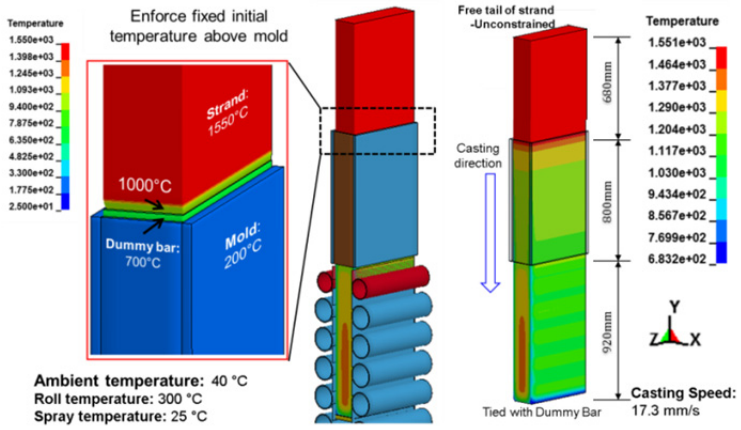

Figure 2: Thermal and mechanical boundary conditions of the model

On mold exit, the strand domain enters secondary cooling zones and experiences alternating periods of: water spray / air mist cooling (convection), roll contact (thermal contact conductance), and slower, ambient-temperature cooling in the regions that are sheltered beneath the rolls (convection and radiation), as shown in Figure 3. The impacted spray water is held fixed at 25 °C, the rolls are at 300 °C, and ambient temperature is 40 °C. In the model, spray cooling convection is applied at specific regions of the strand surface, according to the estimated effective area of the impacted region beneath each spray nozzle. A meshed region was created for each effective spray area, which is fixed in space, and interacts only thermally, and not mechanically, with the chunk domain. That thermal interaction involves applying the convection of that particular spray to the adjacent portion of the moving strand surface, while it is within view.

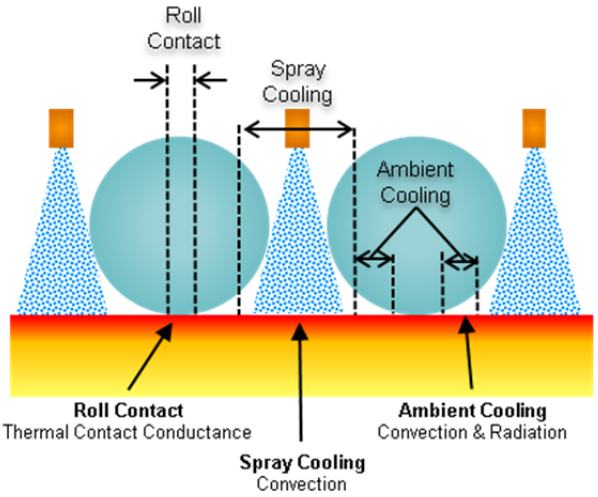

Figure 3: Secondary cooling segment schematic

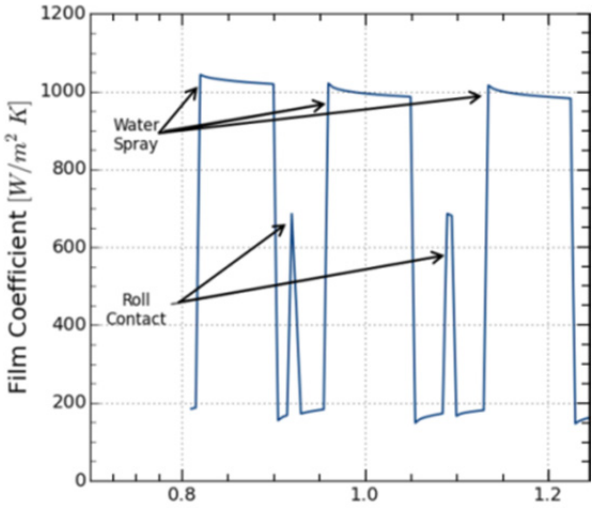

Figure 4: Heat transfer behavior during roll contact and water sprays in secondary cooling

Mechanical Boundary Conditions

The narrow face and wide face mold of the caster domain are vertical and held completely fixed in both space and time. Taper is not applied in the mold. Below the mold, machine taper and changing caster radii, including straight and curved segments for bending and unbending are all applied by fixing the locations of the roll surfaces, based on the caster geometry. Individual rolls are held fixed from translation but are allowed to freely rotate around their center. In this preliminary work, all rolls thus are treated as support rolls and not drive rolls. The outside surface of each roll is allowed to contact the surface of the strand chunk without penetration. To reduce computational complexity, rolls on the inner and outer radii were only given contact constraints with their corresponding strand surface (i.e. inner radius rolls only "see" the inner radius strand surface).

The dummy bar follows a predefined path down the caster at the casting speed of 17.3 mm/s to pull and guide the strand at the correct orientation for steady casting. The dummy bar and strand chunk travel together down the caster through the vertical mold section, bending and unbending, and horizontally out of the caster. The position of the dummy bar at a given time is fixed, based on the casting speed and non-linear arc length calculations based on the caster geometry. Nodes on the bottom of the strand domain are attached to corresponding nodes on the dummy bar domain surface, using "tie constraint" equations. Each node of the strand bottom and dummy bar top surfaces is given an individual local coordinate system, in order to constrain only the degrees of freedom in the casting direction. This enables the large rotations of the strand chunk as its orientation changes, due mainly to rigid body motion, as it moves through the caster during the simulation. This is equivalent to a mechanical symmetry condition applied to the bottom surface of the chunk domain, keeping this planar section perpendicular to the casting direction at all times.

In contrast to the special set of constraints at the strand bottom surface, the top surface of the chunk domain is unconstrained (zero force boundary condition). This allows the entire chunk domain to deform (e.g. liquid to be squeezed in and out) and thus prevents non-physical mass conservation of the domain. These constraint conditions are critical to achieving reasonable mechanical behavior and stress results from the simulation.

Material Properties

During solidification and cooling in this process, the thermal-mechanical properties of the steel vary considerably with temperature and additionally, constitutive models are needed to convert between stress and strain. Material properties such as density, elastic modulus, thermal conductivity, enthalpy, and specific heat are taken from previous work [20]. In this work, an elastic-plastic formulation was adopted, using stress-strain curves for each temperature and phase (liquid, delta-ferrite, austenite) that are strain-rate dependent.

Three different constitutive models were used to define the constitutive property data, based on the three phases of steel, liquid, delta-ferrite, and gamma-austenite. Liquid was modeled as an elastic perfectly plastic weak solid with a yield stress of 10 kPa. For ferrite, the Zhu-power law model was used [21], and for austenite, the Kozlowski model III was used [22]. Examples of the constitutive data are plotted in Figures 5 and 6, for a variety of strains, strain rates, and temperatures, of both solid phases. This model uses a stress-strain form of the constitutive behavior rather than the inelastic-creep type formulation used in prior work [20] but produces similar results.

For a model of this size, efficiency is critical, to help ease the computational difficulty and solve time. Thus, the thermal and mechanical material properties used in this work are a tabular version of data generated from the equations given in previously validated modeling work [20]. Using tables with discrete data for a variety of strains, strain rates, and temperatures LS-Dyna interpolates between the values to find the relevant property. The simulation presented in this work involved a 700,000 node finite-element mesh of 3D thermal-mechanical brick elements, and was solved with LS-Dyna on a workstation computer in ~3 weeks.

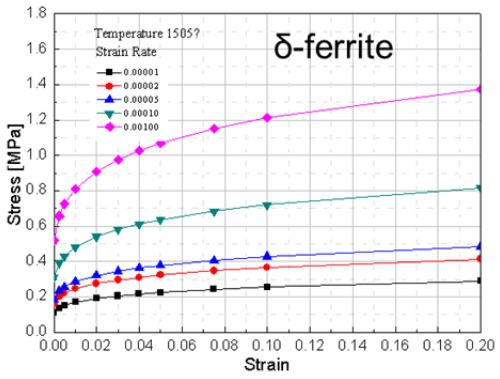

Figure 5: Example constitutive behavior for δ-Ferrite over a variety of strain rates at 1505 °C [21]

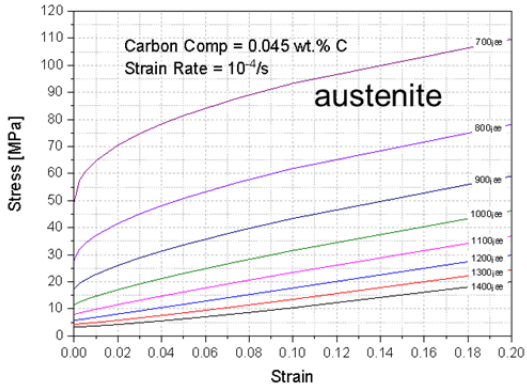

Figure 6: Example constitutive behavior for γ-Austenite over a variety of temperatures at a strain rate of 10^{-4} [21]

RESULTS AND DISCUSSION

Model Validation

Temperature results from the model are shown in Figures 7, 8, and 9. The temperature profile down the caster, the shell growth profile, and the metallurgical length all match remarkably well with prior calculations for the same caster, which was previously shown to match with plant measurements [16].

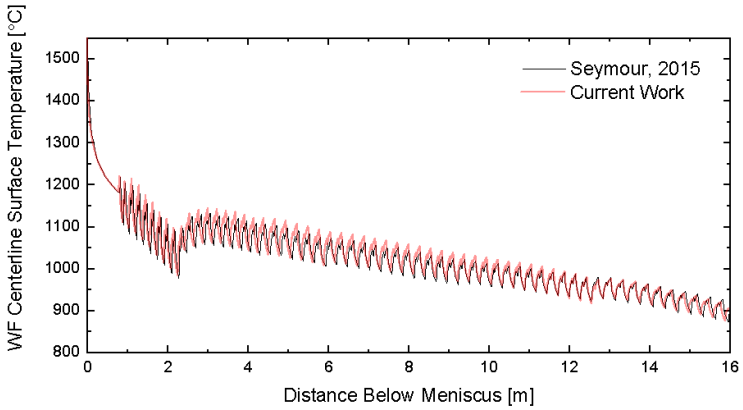

Figure 7: Surface temperature variation down the caster, comparing current 3D model with previous work [16]

Stress profiles taken at the WF centerline (symmetry plane) are shown in Figure 9 and match both qualitatively with accepted solidification stress behavior [23] and quantitatively with previous work using simplified slice models of similar composition and conditions [16], [20], [24].

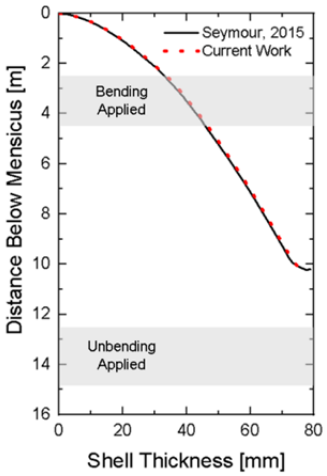

Figure 8: Shell growth profile from current 3D model compared to previous work [16]

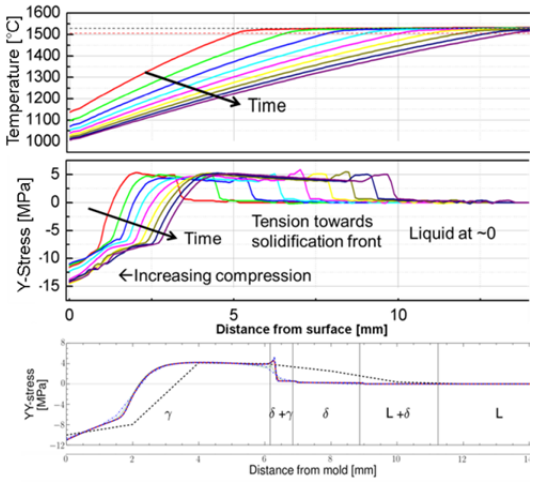

Figure 9: Temperature and hoop stress through the strand thickness from current 3D model at several times, compared with previous work (bottom) 10 seconds below meniscus with lines to show phases [20]

Initial Solidification in the Mold

Thermal-mechanical behavior in the mold is important to subsequent behavior below the mold and surface crack formation. As discussed in previous work [20], fast cooling of the shell surface generates a brief period of tensile stress during early solidification in the mold. As the shell continues to grow, internal cooling and shrinkage accompanied by slower cooling of the surface then causes compressive stress at the surface, increasing to tension towards the solidification front, and dropping to zero in the liquid. This well-known behavior [20], can be observed in Figures 9 and 10. Figure 10 shows that the hoop stress (tangential to the strand surface) increases to over 5 MPa in tension before dropping to ~10 MPa in compression. The second tensile peak is likely due to the shrinkage that accompanies a temporary increase in surface cooling at ~150 mm below the meniscus. This confirms the sensitivity of the hoop-stress condition at the surface to surface cooling conditions, as reported in recent work on stainless steel using a 2D transverse slice model [21].

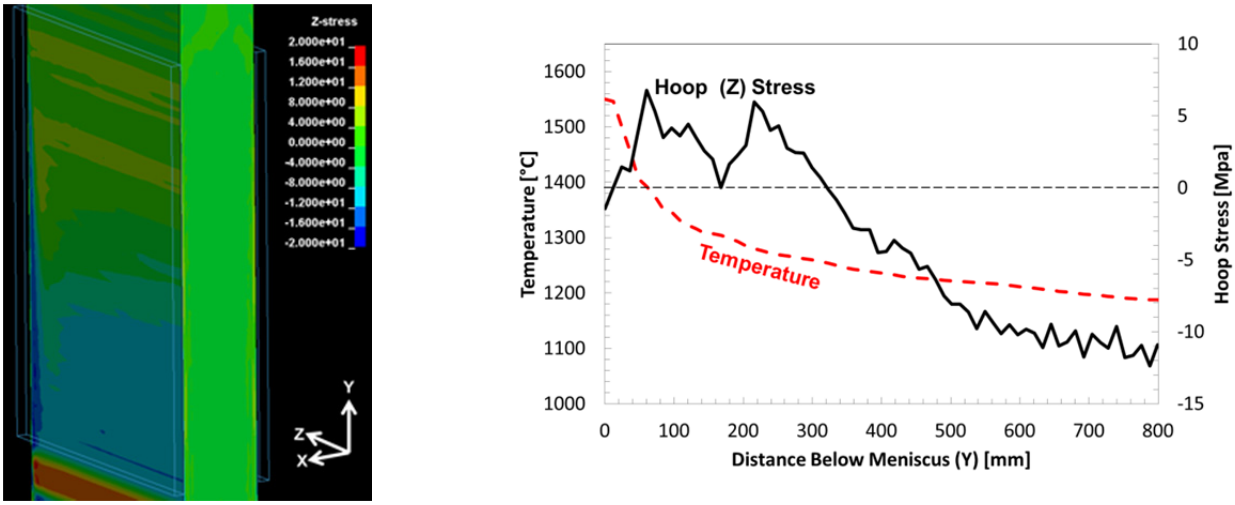

Figure 10: Wide face centerline surface hoop (z) stress (MPa) and surface temperature history in the mold

Spray Cooling and Rolls

Temperature results in Figure 7 show that the strand surface exits the mold just under 1200 °C. The narrow faces then experience prolonged reheating before persistent continuous cooling again (the modeled typical caster does not have NF sprays). As a result of 2-dimensional cooling, the corners are the coldest region around the strand perimeter at any given distance below the meniscus. The wide faces then experience some slight reheating before the first spray zone. This is followed by periodic fluctuations in surface temperature as the strand surface passes beneath the rolls and sprays, which remove substantially more heat than the sheltered regions in between, as shown in Figures 3 and 4. Visible in Figure 7, detail

of these fluctuations are shown in Figure 12a. The spray cooling regions exhibit the largest cooling and lowest surface temperatures, while the adjacent regions (rolls and ambient) experience reheating.

As temperature changes are the cause of thermal stress, the hoop stresses are seen in Figure 12b to fluctuate according to the spray cooling, roll contact, and in-between regions. As described in the previous section, the strand surface exiting the mold is in compression. Sudden cooling of the strand surface by the sprays causes local contraction of that portion of the surface. Mechanical constraint by the surrounding hotter surface and subsurface opposes contraction, so the result is tension beneath the sprays in both the casting direction and strand circumference (hoop) directions, as shown in Figures 11a and Figure 12b. Complementary compression is induced beneath the sprayed region of the strand surface, as well as a slight decrease in the tension near the solidification front.

Figure 12b shows that the tensile hoop stress resulting from the sprays is approximately 15 MPa, prior to bending, with the magnitude increasing with distance below mold. This behavior has been noted in previous work [7], [16]. The qualitative behavior of alternating tension and compression with and without sprays is present throughout the roll containment portion of the caster with increasing magnitude with distance below the mold.

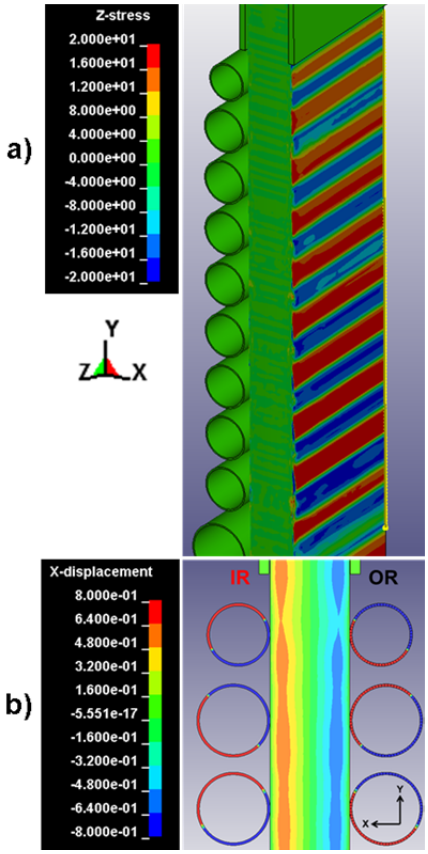

Figure 11: a) Hoop (z) stress (MPa) on the inner radius after mold exit and before unbending, b) Bulging displacement (mm) at wide face centerline between the first 3 support rolls below the mold

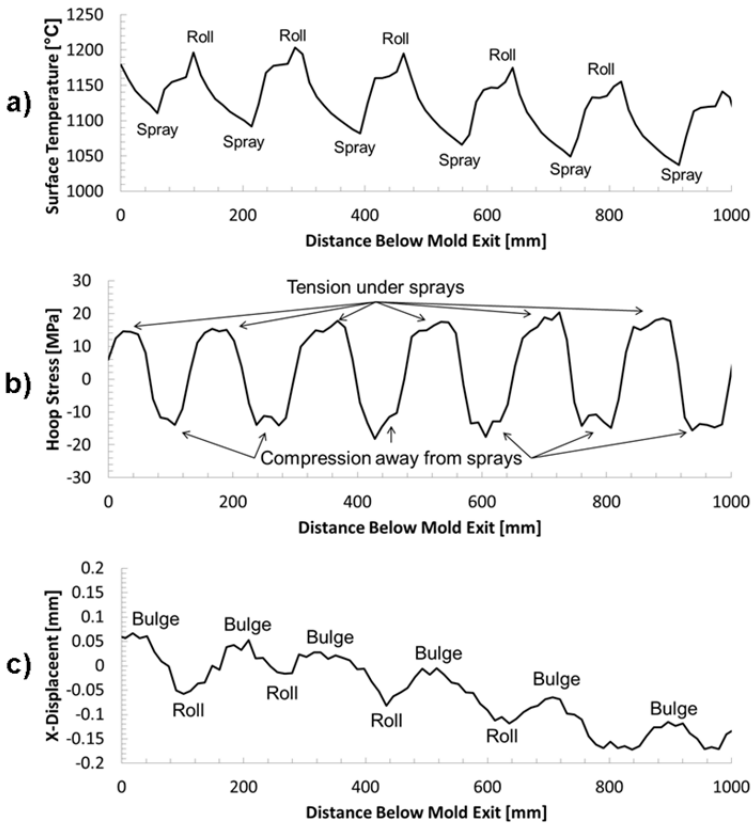

Figure 12: Wide face centerline results at the surface of the inner radius (marked with yellow line: a) Surface temperature, b) Hoop (z) stress, c) Bulging (X) displacement of the inner radius

Figure 13 shows the through-thickness-stress (X-Stress) through the thickness of the strand, prior to bending. This stress is only significant near the corners and on the narrow face. Figure 13a shows that this X-Stress reaches a peak compressive stress directly under each roll right at the corner region. The corresponding stress plot at the wideface centerplane, Figure 13b shows negligible through-thickness stress, as the liquid interior provides no resistance to deformation.

The high stresses in the narrow face, Figure 13a, are caused by the machine taper in this upper portion of the caster being slightly too large and squeezing the strand. While the low (ambient) temperature of the rolls, and their accompanying cooling, shrinkage, and tension-generating effects [16], are included in the model, the mechanical squeezing effect of the rolls was larger in this case. Tension is also observed in the regions surrounding the compression to balance out the forces, these tensile regions may be prone to corner cracking depending on the temperature history of the strand and the brittle temperature regions of the grade being cast. As the coldest part of the slab the corners and the narrow faces experience the highest stresses

during the casting process, and improper machine taper has the potential to cause unnecessary extra difficulties such as premature roll wear, shape problems and off corner cracking.

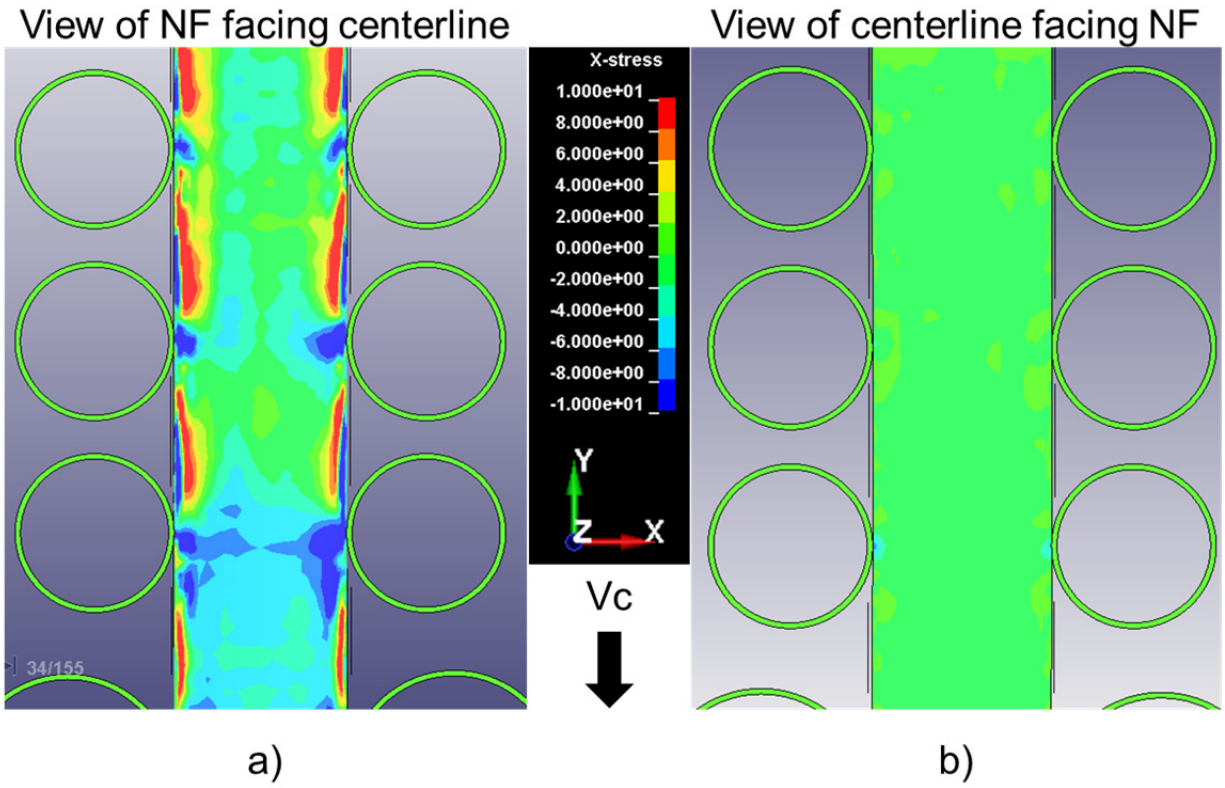

Figure 13: Through-thickness x-stress contours (MPa): a) on narrow face and b) through centerplane before bending

Bulging

Bulging occurs in continuous casting as the internal ferrostatic pressure from the molten core pushes the solid shell outwards against the constraint of the support rolls in the caster. Deformation outwards between rolls increases when the shell is hot and thin, the roll spacing is too large, or if there is roll misalignment. Bulging can lead to many quality problems including unstable mold level fluctuations, transverse cracking, segregation, as well as undue stress on the containment portion of the caster. Bulging is observed between rolls on most of the wide face shell, away from the corners which mechanically constrain the edges of the WF from bulging. As seen in Figures 11b and 12c, bulging between the first 3 support rolls is only ~0.15 mm. This is due to the efficient use of small-diameter, split-rolls in this caster, which enable a small roll pitch. There is some bulging present in the mold, as this model does not include any taper of the wide face coppers. However, machine taper of the rolls down the caster is included, which causes the general downward slope of Figure 12c. Recall that the machine taper in this caster caused the through-thickness stress observed in Figure 13.

Bending and Unbending

The strand in this vertical-mold caster experiences multipoint bending into the constant radius of the caster arc, followed later by unbending after the entire strand has solidified. This introduces complex stress states to the strand, which are captured by the 3D model. During mechanical bending of the 4-sided box-shaped solid shell with its liquid core, the shell on the inner radius of the wideface is forced into compression, with corresponding tension generated in the outer radius shell. These stresses are highest in the casting direction, as expected from Euler-Bernoulli beam behavior. These casting-direction stresses are shown in Figure 14 through the strand thickness at the wide face centerline. The results from a previous 2D model with a highly refined mesh (a) and the current 3D model (b) show that this mechanical effect generally dominates over the superimposed alternating tension and compression experienced by the shells on the inner and outer radius, due to the alternating surface temperatures caused by the sprays and rolls. The central liquid region naturally remains at nearly zero stress. Note that there are also some minor variations in the stress profile caused by the marginal mesh resolution of the current 3D model.

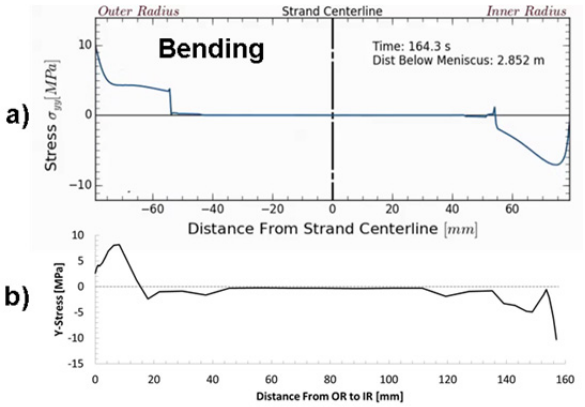

Figure 14: Casting direction (Y) stress through the thickness at the wide face centerline during bending (with a liquid core): a) From a previous 2D model [16] b) From the current 3D model

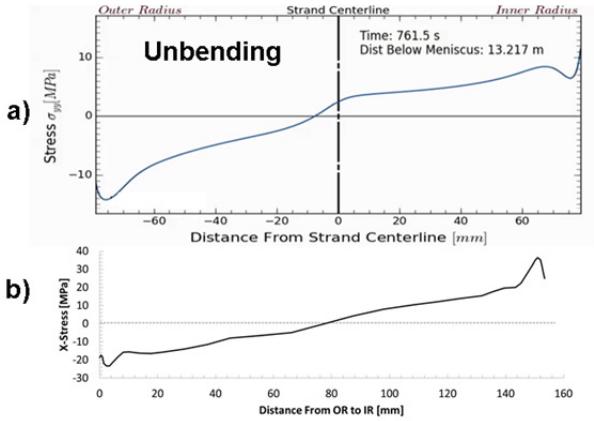

Figure 15: Casting direction (X) stress through the thickness at the wide face centerline during unbending (with a solid core): a) From a previous 2D model [16] b) From the current 3D model

Unbending is experienced later by the strand, after moving through the constant-machine-radius majority of the contained region of the caster. Note that as the strand orientation changes from vertical during bending to horizontal during unbending, the casting-direction stress changes from Y to X. Figure 15 shows casting direction (X) stress through the thickness at the wide face centerline during unbending, again for the previous model (a), and the current work (b) which again show a reasonable qualitative match. As expected from beam theory, the stress profile reverses to compression near the outer radius and tension near the inner radius. At this time, the strand is completely solid in this caster, so the stresses are expected to be higher, as the results show, and they generally increase continuously from compression at the outer radius towards tension at the inner radius. Local stress very near to the strand surfaces jump sharply between tension and compression according to the local condition of cooling or reheating at the strand surface.

Figure 16 and 17 show hoop (Z width direction) stress at the wide face centerline, underneath and away from a spray, during bending and unbending respectively. The tension induced by the rapid cooling from sprays is enough to completely reverse the stress behavior and drive the surface of the strand into tension. Note that tension developing beneath the sprays at the surface in the width direction (Z-stress in Figure 17) is higher than in the casting direction (X-stress in Figure 15). This is because the fan-shaped sprays cause a wider region of the strand to shrink in the width direction.

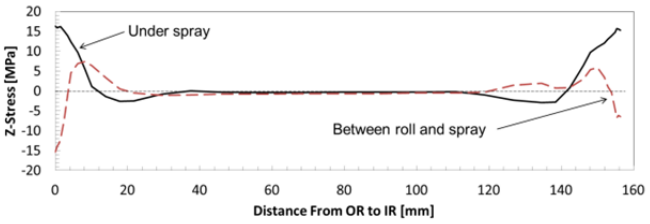

Figure 16: Hoop (z) stress through the thickness at the wide face centerline during bending under a sprayed and unsprayed region

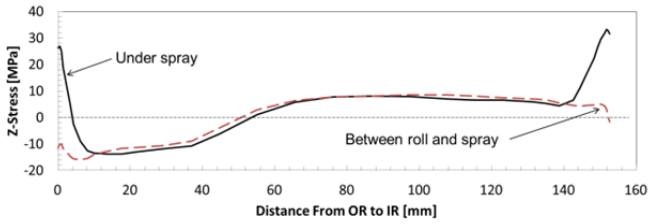

Figure 17: Hoop (z) stress through the thickness at the wide face centerline during unbending under a sprayed and unsprayed region

The effect of bending and unbending on casting-direction stress development at the narrow face surfaces is shown in Figures 18-21. Generally, the behavior matches expectations for bending and unbending a single beam with a solid core: the inner radius gets compressed and the outer radius experiences tension during bending; and the opposite occurring during unbending. However, the distribution of these stresses is slightly more complicated, especially near the corners, owing to the additional effects of the alternating tension and compression from the spray cooling regions, and the local compression beneath the rolls due to squeezing from the machine taper.

Due to the lower temperatures, as well as the extra constraint, the narrow faces experience higher stresses than the center, especially during bending. This can be seen by comparing the magnitudes of the casting direction stress at the narrow face in Figure 19 with the corresponding magnitudes at the centerline in Figure 14. In bending, mostly symmetrical compressive stress is observed near individual rolls with the peaks found on either side of the roll contact.

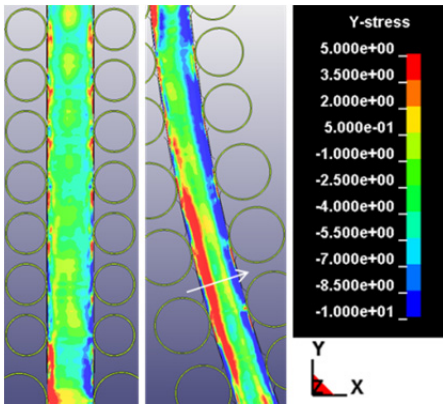

Figure 18: Casting direction stress on the narrow face just before and during bending

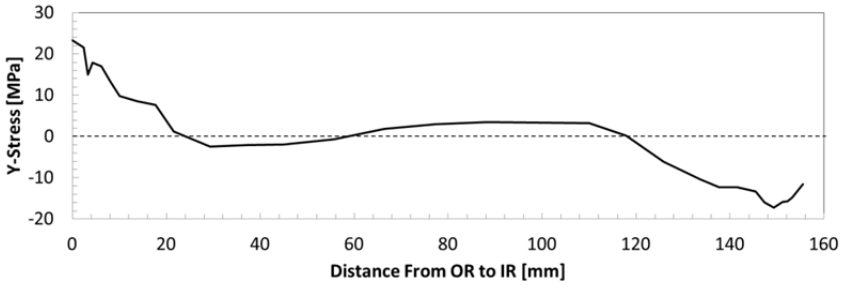

Figure 19: Casting direction stress through the thickness along the narrow face surface during bending (indicated by white arrow in Figure 17)

The stress in the casting directions at the narrow face during unbending experiences much higher tension on the inner radius and compression on the outer radius. Again, the magnitudes of the casting direction stress at the narrow face, Figure 21, are substantially higher than that at the centerline, Figure 15. The tensile stress on the inner radius is centered around the second roll of the unbending section, as shown in Figure 20, which suggests that most of the work of unbending is being accomplished by the first two rolls in the segment.

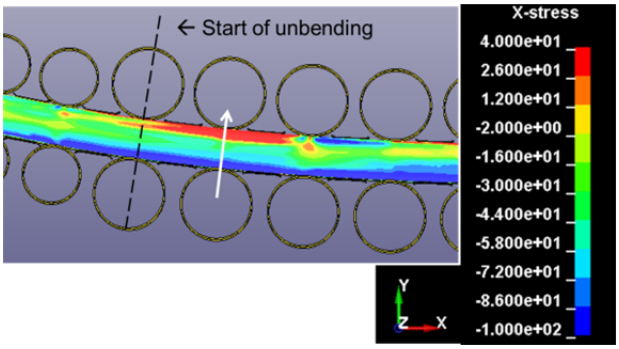

Figure 20: Stress in the casting direction on the narrow face during unbending

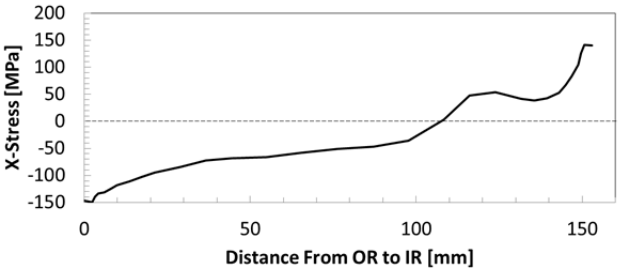

Figure 21: Stress in the casting direction through the thickness at the narrow face surface during bending (indicated by white arrow in Figure 19)

Bending and unbending also affects the shape of the strand. During casting, the entire strand is trying to shrink towards the center of the cross section. This is shown for the width direction in Figure 22, where both corners (at the narrow face) are observed to shrink (negative displacement). The inner and outer radii behave differently, however. During bending, as the inner radius surface is being compressed in the casting direction, it tries to expand in the width direction, in an attempt to conserve volume (surface area). At the same time, as the outer radius is stretched in the casting direction, it consequently shrinks slightly in the width direction. This deformation results in a trapezoidal cross sectional shape (wider inner radius) as the strand attempts to conserve volume. The accompanying contribution of this behavior to the width-direction hoop stress appears to be less than the effect of the sprays.

Finally, during unbending, the trapezoid shape tries to reverse with the opposite behavior: contraction of the strand inner-radius width and expansion of the outer radius. Owing to the strand being totally solid, this only partially occurs, and a slight trapezoidal shape remains in the final slab. The accompanying result of this unbending effect does lead to a general reversal of stress in the strand interior, as Figure 17 shows compressive hoop stress towards the outer radius and tensile hoop stress towards the inner radius.

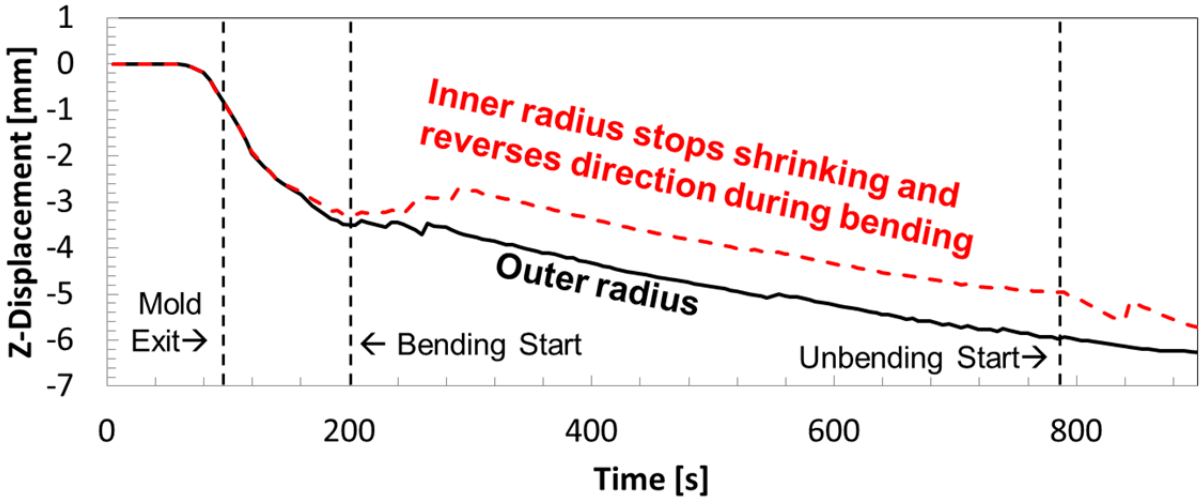

Figure 22: Width-direction shrinkage towards the WF centerline (Z-displacement at the corners)

CONCLUSIONS

A fully three-dimensional transient Lagrangian thermal-mechanical finite-element model of the entire continuous slab casting process has been developed using LS-Dyna. The model has been applied to simulate the behavior of a 2.4 m long chunk of the strand in a typical thick slab caster from initial solidification in the mold, through secondary cooling and containment, past final solidification at the metallurgical length, and includes the effects of spray cooling, bulging between rolls, bending and unbending, machine taper, and other important phenomena.

The model results illustrate the surface temperature drops, and the accompanying shrinkage and tensile hoop stresses that develop as periodic bands across the wide-face surfaces due to spray water impingement, and the corresponding compression bands that arise in the unsprayed regions near roll contact. The outer-radius tension during bending, inner-radius tension during unbending, and bulging between rolls are also simulated. The strand corners experience the highest stresses due to their lower temperature. Squeezing due to machine taper generates slight compression peaks beneath regions of roll contact, but only near the narrow faces when there is a liquid core. During bending, the strand exhibits beam bending behavior, with tension on the OR and compression on the IR, with the opposite trends appearing during unbending with substantially higher magnitude. It is also found that on bending, the shape of the cross section of the strand changes from a rectangle into a trapezoid with a wider inside radius, which persists past final solidification and unbending. It is also seen that each segment has a characteristic stress behavior related to the configuration of the water sprays and the rolls.

FUTURE WORK

This model is a first attempt to include the important phenomena that govern thermal-mechanical behavior in the entire continuous-slab casting process into a single comprehensive model. Much future work and analysis is needed, however. The quantitative accuracy of the current model is limited by mesh discretization issues, as the element size is too coarse. In addition to improving mesh refinement, the length of simulated chunk should be increased, in order to simulate stress evolution properly through startup to steady-casting conditions. Exploring novel operational practices such as compression casting is possible with this type of model and is intended as future work already underway. The model has great potential to study important phenomena, including bulging based on roll pitch and segment length, soft reduction practices, steel grade effects, and extending the model to investigate crack formation, segregation, and other issues that affect steel continuous casting.

ACKNOWLEDGEMENTS

The authors wish to thank the members of the Continuous Casting Center at the Colorado School of Mines as well as The China Scholarship Council (No.201606465036) for providing financial support. Additionally, the authors would like to acknowledge the contribution of Nathan Seymour for his 2D modeling work on this topic.

REFERENCES

1. Y. Feng and A. B. Phillion, “A 3D Meso-Scale Solidification Model for Steels,” vol. m, no. 905.
2. A. Teskeredžić, I. Demirdžić, and S. Muzaferija, “Numerical Method For Heat Transfer, Fluid Flow, And Stress Analysis In Phase-Change Problems,” *Numer. Heat Transf. Part B Fundam.*, vol. 42, no. 5, pp. 437–459, Nov. 2002.
3. B. G. Thomas, S. Koric, L. C. Hibbeler, and R. Liu, “Multiphysics Model of Continuous Casting of Steel Beam-Blanks,” in *InSteelCon*, 2011, vol. 56, no. 5–6, pp. 1–10.
4. L. Yu, “FEM Analysis of Bulging Between Rolls in Continuous Casting,” Masters Thesis, The University of Illinois at Urbana-Champaign, 2000.
5. J. B. Dalin and J. L. Chenot, “Finite element computation of bulging in continuously cast steel with a viscoplastic model,” *Int. J. Numer. Methods Eng.*, vol. 25, no. 1, pp. 147–163, 1988.
6. A. Yoshii and S. Kihara, “Analysis of Bulging in Continuously Cast Slabs by Bending Theory of Continuous Beam,” *Trans. Iron Steel Inst. Japan*, vol. 26, no. 10, pp. 891–894, 1986.
7. M. Bellet and A. Heinrich, “A two-dimensional finite element thermomechanical approach to a global stress -strain analysis of steel continuous casting,” *ISIJ Int.*, vol. 44, no. 10, pp. 1686–1695, 2004.
8. K. H. Tacke, “Multi-Beam Model for Strand Straightening in Continuous Casting,” *Ironmak. Steelmak.*, vol. 12, no. 2, pp. 87–94, 1985.
9. K. Schwaha, E. Till, J. Stulik, and B. Lindorfer, “Continuous Strand Bending and Straightening with Voest Alpine Concept - A Comparative Study,” in *Continuous casting ’85 : Proceedings of the international conference*, 1985, p. 4.1-4.3.
10. Uehara, I. V. Samarasekera, and J. K. Brimacombe, “Mathematical Modelling of Unbending of Continuously Cast Steel Slabs,” *Ironmak. Steelmak.*, vol. 13, no. 3, pp. 138–153, 1986.
11. F. Pascon and A. M. Habraken, “Finite element study of the effect of some local defects on the risk of transverse cracking in continuous casting of steel slabs,” *Comput. Methods Appl. Mech. Eng.*, vol. 196, no. 21–24, pp. 2285–2299, Apr. 2007.
12. M. Deisinger and K.-H. Tacke, “Unbending of Continuously Cast Slabs with Liquid Core,” *Ironmak. Steelmak.*, vol. 24, no. 4, pp. 321–328, 1997.
13. Y. Zhao, D. F. Chen, M. J. Long, J. L. Shen, and R. S. Qin, “Two-dimensional heat transfer model for secondary cooling of continuously cast beam blanks,” *Ironmak. Steelmak.*, vol. 41, no. 5, pp. 377–386, 2014.
14. R. Moravec, K. E. Blazek, J. Horsky, C. Graham, S. Fiegle, T. Dombovic, and T. Kaurich, “Coupling Of Solidification model And Heat Transfer Coefficients to Have Valuable Tool for Slab Surface Temperatures Prediction,” in *InSteelCon*, 2011, no. July, pp. 1–9.
15. J. Horsky and J. Ondrouskova, “Analysis of Directly Measured Heat Transfer Coefficients During Special Experiments to Provide Better Understanding of Secondary Cooling During Continuous Casting Process,” in *AISTech - Iron and Steel Technology Conference Proceedings*, 2013.
16. N. M. Seymour, “Thermo-Mechanical Behaviorof Steel in the Continuous Casting Process From Meniscus to Caster Exit,” Masters Thesis, The University of Illinois at Urbana-Champaign, 2016.
17. R. Hardin, P. Du, and C. Beckermann, “Three-dimensional Simulation of Heat Transfer and Stresses in a Steel Slab Caster,” in *InSteelCon*, 2011, no. July, pp. 1–6.
18. R. A. Hardin and C. Beckermann, “Heat Transfer and Solidification Modeling of Continuous Steel Slab Casting,” in *Proceedings of the 2nd International Symposium on the Recent Developments in Plate Steels*, 2018, pp. 21–31.
19. L. S. T. Corporation, “LS-DYNA.” Lawrence Livermore National Laboratory, 2015.
20. M. L. S. Zappulla, L. C. Hibbeler, and B. G. Thomas, “Effect of Grade on Thermal–Mechanical Behavior of Steel During Initial Solidification,” *Metall. Mater. Trans. A*, vol. 48, no. 8, pp. 3777–3793, Aug. 2017.
21. M. L. S. Zappulla, S. Koric, S.-M. Cho, H.-J. Lee, S.-H. Kim, and B. G. Thomas, “Multiphysics Modeling of Viscoplastic Behavior of Solidiying Stainless Steel During Continuous Casting,” *J. Mater. Process. Technol. (Submitted Febr. 2019)*.
22. P. F. Kozlowski, B. G. Thomas, J. A. Azzi, and H. Wang, “Simple constitutive equations for steel at high temperature,” *Metallurgical and Materials Transactions A*, vol. 23. pp. 903–918, 1992.

23. J. H. Weiner and B. A. Boley, “Elasto-plastic thermal stresses in a solidifying body,” *J. Mech. Phys. Solids*, vol. 1, no. 3, pp. 145–154, 1963.

24. M. L. S. Zappulla, “Grade Effects on Thermal-Mechanical Behavior During the Initial Solidification of Continuously Cast Steels,” Masters Thesis, The University of Illinois at Urbana-Champaign, 2016.

